
Article:
Holsgrove, Kristina M., Kepaptsoglou, Demie M. orcid.org/0000-0003-0499-0470, Douglas, Alan M. et al. (7 more authors) (2017) Mapping grain boundary heterogeneity at the nanoscale in a positive temperature coefficient of resistivity ceramic. Materials. 066105. pp. 1-11. ISSN 1996-1944

https://doi.org/10.1063/1.4989396

Mapping grain boundary heterogeneity at the nanoscale in a positive temperature coefficient of resistivity ceramic

Kristina M. Holsgrove, Demie M. Kepaptsoglou, Alan M. Douglas, Quentin M. Ramasse, Eric Prestat, Sarah J. Haigh, Michael B. Ward, Amit Kumar, J. Marty Gregg, and Miryam Arredondo

Citation: APL Materials **5**, 066105 (2017);
View online: https://doi.org/10.1063/1.4989396
View Table of Contents: http://aip.scitation.org/toc/apm/5/6
Published by the American Institute of Physics

Mapping grain boundary heterogeneity at the nanoscale in a positive temperature coefficient of resistivity ceramic

Kristina M. Holsgrove,[1] Demie M. Kepaptsoglou,[2] Alan M. Douglas,[1] Quentin M. Ramasse,[2] Eric Prestat,[3] Sarah J. Haigh,[3] Michael B. Ward,[4] Amit Kumar,[1] J. Marty Gregg,[1] and Miryam Arredondo[1,a]

[1]*Centre for Nanostructured Media, School of Mathematics and Physics, Queen's University Belfast, University Road, Belfast BT7 1NN, United Kingdom*

[2]*SuperSTEM Laboratory, STFC Daresbury, Keckwick Lane, Daresbury WA 4AD, United Kingdom*

[3]*School of Materials, University of Manchester, Manchester M13 9PL, United Kingdom*

[4]*Institute for Materials Research, School of Process, Environmental and Materials Engineering, University of Leeds, Leeds LS2 9JT, United Kingdom*

(Received 27 September 2016; accepted 8 June 2017; published online 21 June 2017)

Despite being of wide commercial use in devices, the orders of magnitude increase in resistance that can be seen in some semiconducting $BaTiO_3$-based ceramics, on heating through the Curie temperature (T_C), is far from well understood. Current understanding of the behavior hinges on the role of grain boundary resistance that can be modified by polarization discontinuities which develop in the ferroelectric state. However, direct nanoscale resistance mapping to verify this model has rarely been attempted, and the potential approach to engineer polarization states at the grain boundaries, that could lead to optimized positive temperature coefficient (PTC) behavior, is strongly underdeveloped. Here we present direct visualization and nanoscale mapping in a commercially optimized $BaTiO_3$–$PbTiO_3$–$CaTiO_3$ PTC ceramic using Kelvin probe force microscopy, which shows that, even in the low resistance ferroelectric state, the potential drop at grain boundaries is significantly greater than in grain interiors. Aberration-corrected scanning transmission electron microscopy and electron energy loss spectroscopy reveal new evidence of Pb-rich grain boundaries symptomatic of a higher net polarization normal to the grain boundaries compared to the purer grain interiors. These results validate the critical link between optimized PTC performance and higher local polarization at grain boundaries in this specific ceramic system and suggest a novel route towards engineering devices where an interface layer of higher spontaneous polarization could lead to enhanced PTC functionality. [http://dx.doi.org/10.1063/1.4989396]

The Positive Temperature Coefficient of Resistivity (PTCR) effect is a property found in polycrystalline materials which produce a switch from a low resistance semiconducting state to a higher state of resistance in response to either internal or external heating. Understandably, this effect has found extensive applications in sensing technologies such as self-regulating heating elements, current sensors, and sensors for the detection of air flow, liquid level, and temperature changes.[1] Among the various materials exhibiting a PTCR effect to date, the most favored material group is $BaTiO_3$ (BTO) based compounds where the temperature at which this switch in behavior occurs, near the ferroelectric-paraelectric Curie transition temperature (T_C), and the magnitude of the switch can be controlled and optimized via the addition of different dopants and/or changes in the processing conditions.[2,3]

[a]Author to whom correspondence should be addressed: m.arredondo@qub.ac.uk

Over the past 50 years, research on the PTCR effect has focused on compositional and structural issues that govern the electrical properties.[4,5] It was identified quite early that the effect is dominant in polycrystalline samples,[6] with rich microstructures and an equally interesting domain structure embedded within grains, and several models have been proposed to explain the observed experimental behavior.[7–10] The most accepted among these models is the Heywang-Jonker model, which states that the presence of a potential barrier at the grain boundaries is responsible for enhanced resistivity of the boundary in comparison to the grain interior. According to the original Heywang model[7] (reviewed by Chen and Yang[4]), there is a bi-dimensional layer of electron traps, i.e. acceptor states, along the grain boundaries of BTO, which exhibits different electrical properties from those of the bulk phase. A two-dimensional electron trap exists along the grain boundary where acceptor states attract electrons from the bulk resulting in an electron depletion layer and consequently a potential barrier. The barrier at the grain boundary (ϕ_0) is given by

$$\phi_0 = \frac{e^2 N_s^2}{8\,\varepsilon_0 \varepsilon_{gb} N_0}, \tag{1}$$

where e refers to electron charge, ε_0 is the permittivity of free space, ε_{gb} is the permittivity of the grain boundary region, N_s is the concentration of surface acceptor states, and N_0 is the concentration of charged species in the depletion layer. The overall resistivity ρ is then determined by the barrier height and given by

$$\rho = A e^{\frac{\phi_0}{kT}}, \tag{2}$$

where k refers to the Boltzmann constant and A is a geometrical factor. As evident from Eq. (2), the overall resistivity exhibits the same trend as the barrier height. While the Heywang model provided some insight into the PTCR behaviour, it was unable to explain the PTCR behaviour below T_C.

Jonker modified Heywang's model by incorporating the ferroelectric nature of the material with the possibility that different grains have different polarisation orientations.[8] In fact, each grain itself can have different domains in it and thus a wide range of possibilities emerges, in terms of polar discontinuities present at the grain boundaries. Surface charges are generated when the net polarisation vector normal to grain boundaries is created. Negative surface charges diminish the potential barrier while the barrier for domains with positive surface charges increases. The conducting electrons always follow the path with the lowest barriers so that the material as a whole has low resistivity. According to the modified Heywang-Jonker model,[5] the barrier potential (ϕ) observed at the grain boundary is given by

$$\phi = \frac{e^2 N_s^2 - (\Delta P_n^2 + \Delta P_z^2)}{8\,\varepsilon_0 \varepsilon_{gb} N_0}, \tag{3}$$

where ΔP_n is the component of spontaneous polarisation normal to the grain boundary, and ΔP_z represents the polarisation generated due to stresses at the grain boundaries as considered by Kulwicki and Purdes.[10] This model takes into account the ferroelectric nature of the material and postulates that the spontaneous polarization below T_C, or more appropriately the polar discontinuity arising from domain structures, effectively lowers the potential barrier in the vicinity of grain boundaries, thus lowering the resistivities below T_C. It should be noted that the grain boundary is always more resistive than the interior of the grains, even in the ferroelectric (low resistance) phase. As the material undergoes the ferroelectric-paraelectric transition, domains disappear and with no influence of polarization, depletion regions and resistive barriers at the grain boundaries are restored leading to a high resistance state. The polarization discontinuity at the boundary and its origin, particularly from the underpinning ferroelectric domain structure, have been an ongoing topic of debate in BTO-based PTCR ceramics.[5,11] A better understanding of the link between magnitude of polar discontinuity and enhanced PTC behavior could help optimize the PTCR behavior and allow development of novel routes towards engineering higher local polarization discontinuities at grain boundaries.

Most of the experimental evidence towards the role of grain boundaries in enhanced PTCR behavior is based on macroscopic studies employing techniques such as impedance spectroscopy, which allows the interpretation of grain-boundary resistivity in terms of equivalent circuit diagrams.[12,13] However, direct analysis of grain boundaries linked to PTCR behavior on the nanoscale that could unequivocally establish the clear role of grain boundaries has been limited in previous studies.[14]

There is also the open question of chemical inhomogeneity and segregation at grain boundaries, and how these relate to polarization discontinuity. Several studies have suggested that chemical diffusion and segregation at the grain boundaries are responsible for the PTCR effect, but attempts to provide evidence of this chemical heterogeneity have so far been unsuccessful.[15–17] Moreover, the most accepted models do not consider clear links between chemical heterogeneity and polarization discontinuity at grain boundaries. Therefore, there is an evident need to investigate the chemistry at the grain boundaries in these complex microstructures, and its role in the modification of potential barriers while preserving the original domain structure at the interface, so that direct evidence of this correlation may be established.

In this context, nanoscale studies aimed at visualization of local resistivity or potential barriers at grain boundaries using scanning probe microscopy based techniques have been challenging due to polishing related issues which can seriously influence the domain structure in these ceramics. To address these issues, grain boundaries possessing one of the clearest reported ferroelectric domain structures have been investigated in this work.[18] Here, we have studied the chemical variations and associated changes in electronic structure across grain boundaries in a BTO based commercially available PTCR ceramic. The ceramic is composed of $BaTiO_3$–$PbTiO_3$–$CaTiO_3$ (BTO-PTO-CTO) where the percentage concentrations are 68%, 20%, and 12% respectively, with an average measured grain size diameter of 4 μm. Pb is commonly added to BTO PTCR ceramics to modify the T_C for relevant applications,[19] while Ca is employed to achieve refinement of grains.[20] The ceramics typically have relatively low bulk resistivity at room temperature (10–100 Ω cm) which increases by up to 4 orders of magnitude, on heating through T_C. Kelvin probe force microscopy (KPFM), a non-contact scanning probe microscopy technique, was employed to establish the central role that grain boundaries play in the PTCR behavior exhibited by these ceramics.

As previously discussed, early studies of PTCR ceramics have mainly been focused on macroscopic scale measurements such as impedance spectroscopy. The use of large electrodes during these investigations, however, precludes the exact determination of the grain boundaries' role in the PTCR effect due to an averaging of their behavior. It would appear obvious that the cleanest way to gain experimental insight into the electrical behavior of these elements would be to investigate them at a local scale, especially in a lateral geometry where the boundaries themselves form elements of the conduction circuit. To realize this scenario, samples were prepared from bulk by cutting and polishing using diamond paper and a colloidal silica solution. Figure 1(a) shows a scan of the topography of the polished surface. While the topography contains hints of underlying domain structure, the domain structure becomes clearly evident in the derivative of the topography shown in Fig. 1(b). Piezoresponse force microscopy (PFM) in both vertical and lateral modes was employed to investigate the local piezoresponse signal associated with the domains [Figs. 1(c) – 1(f)]. The PFM data reveal a rich and complex domain structure showing distinct discontinuities in polar arrangements at the grain boundaries. The domain junctions at the boundaries should correspondingly generate the full range of ΔP values, consistent with the Heywang-Jonker model, where the maximum extent of barrier lowering is due to the maximum possible magnitude of polar discontinuity [Eq. (3)].

Direct spatial mapping of potential barriers across grain boundaries would allow insight into the crucial role that boundaries play in determining the PTCR behavior. In principle, conductive atomic force microscopy (c-AFM) could be used to measure the local current upon the application of a fixed voltage and thus determine the local resistance/barrier at the boundary. Indeed, prior efforts to map currents in PTCR ceramics using c-AFM have shown that the grain boundaries are more resistive than the grains.[21,22] However, recent work by Douglas *et al.*[18] on the PTCR ceramic samples discussed in this study has shown that the c-AFM data is strongly influenced by the nature of the Schottky barrier that develops at the tip-sample interface and thus was deemed unsuitable for assessing the fundamental resistivity of the material. A more direct way of mapping potential drops (and hence inferring local resistance) on the nanoscale is through the use of scanning Kelvin probe force microscopy (KPFM). To investigate the role of grain boundaries in a lateral geometry where they form part of the electrical circuit, KPFM was therefore performed on the polished samples. Au electrodes were sputtered, forming an inter-electrode gap of 80 μm, to allow the application of an in-plane electric field whilst measuring the change in potential across the surface of the material. Figure 2(a) shows the resulting topography for the KPFM experiment, and grain boundaries are

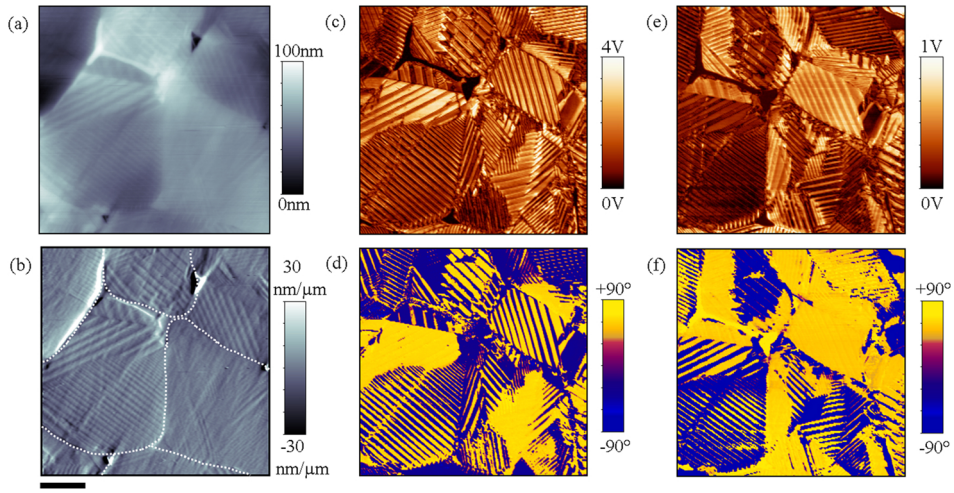

FIG. 1. PFM imaging of domains. A 10 μm × 10 μm scan of topography (a) and its derivative (b) of a polished BTO-PTO-CTO sample. In (a) the scale bar represents 2 μm and the dotted lines in (b) mark a rough outline of grain boundaries. The lateral PFM of amplitude (c) and phase (d), along with the vertical PFM of amplitude (e) and phase (f), shows an intricate series of domains within each grain at the surface. Domains are clearly evident in the derivative of topography. In both sets of PFM scans 2 V AC was applied with the PFM amplitude scale of the lateral signal ranging from 0 V to 4 V, and 0 V to 1 V for vertical.

highlighted with black dashed lines in a schematic of the scanned structure [Fig. 2(b)], allowing for ease of reference. During the experiment, −10 V DC was applied from the right electrode, with respect to the KPFM image, and in the 15 μm region scanned, a change in potential of roughly 1.5 V DC was observed. Typically, when a lateral electric field is applied to a material with homogeneous

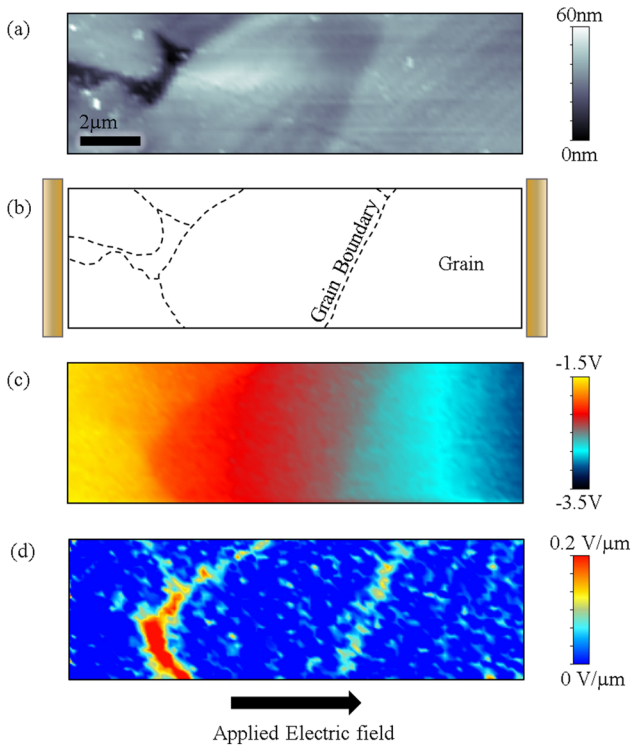

FIG. 2. Topography of the BTO-PTO-CTO surface for the KPFM experiment (15 × 5 μm), with Au electrodes placed parallel to the vertical scan direction (a). Schematic of the scanned area (b). Potential map acquired by applying −10 V across the surface of the sample, measured using KPFM (c) and negative gradient of the potential map (d).

electrical properties, the change in potential is linear, but in this ceramic, the potential map in Fig. 2(c) illustrates that there are distinct areas of non-linear change.

To elucidate the exact location of the largest change in electrostatic potential, the negative gradient of the potential along each horizontal scan line was calculated. Figure 2(d) reveals that the largest drop of potential occurs at the grain boundaries, a result which confirms that these interfaces are indeed much more resistive than the bulk (interior) of the grain. The ratio of the derivatives of potential gradients across the grain boundaries and grains can be used to estimate the ratio of their resistivities using a series resistance model. Using this estimate, the ratio of the resistivities at the grain boundary (ρ_b) and grain (ρ_g) can then be expressed in terms of the effective barrier height (E_b) such that $E_b = kT\ \ln(\rho_b/\rho_g)$. This value of the barrier height at the grain boundary is estimated to be ~ 35 meV which is well within the range of thermal activation at room temperature. Overall the presence of resistive grain boundaries is consistent with models proposed for the electrical structure of the grains using impedance analysis[23] and other techniques.[14,21] While this result is almost expected based on various models, local measurements showing resistive boundaries at room temperature with an applied electric field in this lateral geometry have hitherto not been carried out directly. The concentration of potential contours at the grain boundaries provides direct evidence towards the existence of resistive boundaries and highlights them as the clear regions of interest. To further investigate the nature of these regions, their structural and chemical inhomogeneity was studied on the atomic scale, using high resolution transmission electron microscopy (TEM) techniques.

As a first approach to study the chemical distribution across grain boundaries, electron energy loss spectroscopy (EELS) elemental maps were acquired. An overview of a typical specimen, a focused ion beam cross-section, containing several randomly oriented grains is shown in Fig. 3(a), with grain boundaries marked by white dashed lines. Representative boundaries, such as that in Fig. 3(b) between grains oriented in directions close to the 110 and 210 zone axes, were chosen. EELS maps were acquired on an aberration corrected Nion UltraSTEM 100 at the SuperSTEM facility. Rather than aligning the specimen along one of the main crystallographic axes, it was carefully

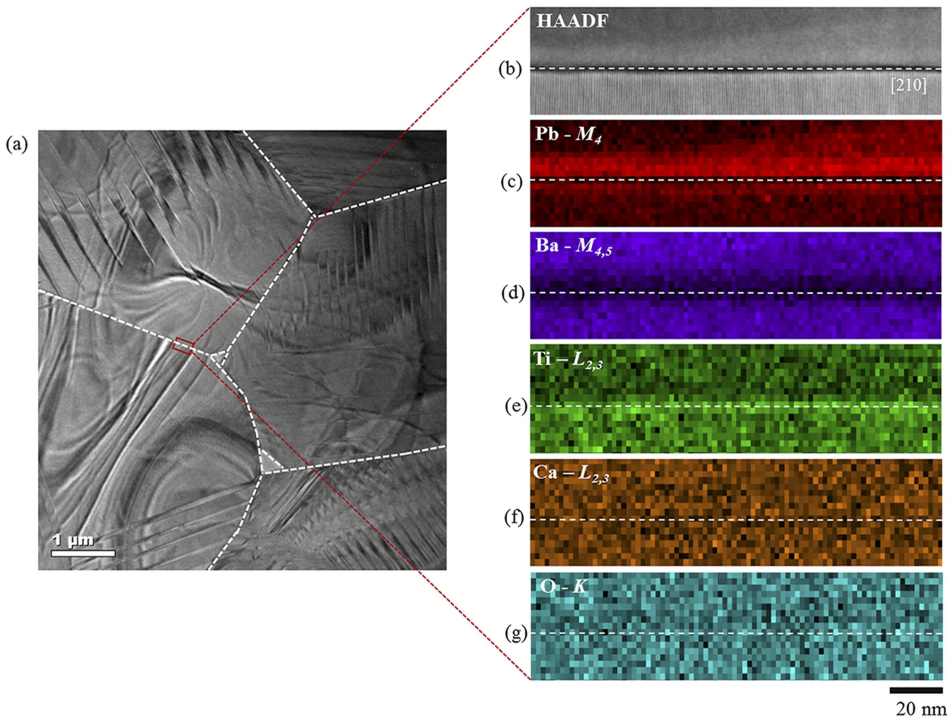

FIG. 3. Chemical distribution across grain boundaries. Bright field TEM overview of various grains used for STEM-EELS analysis (a), where a polydomain structure can be seen within each grain. HAADF image of a single grain boundary where the bottom grain is tilted on the zone axis (b). The grain boundary shows a dark contrast and is marked by a white dashed line. EELS elemental maps for Pb-M_4 (c), Ba-$M_{4,5}$ (d), Ti-$L_{2,3}$ (e), Ca-$L_{2,3}$ (f), and O-K (g).

oriented in the microscope to align the grain boundary parallel to the electron beam (edge-on, to unambiguously reveal the chemical changes across the boundary without projection effects). The microscope was operated in scanning transmission electron microscope (STEM) mode at 100 kV, equipped with a cold field emission gun and a Gatan Enfina spectrometer. A dispersion of 1 eV/channel was used in order to simultaneously acquire the Pb-M_4, Ba-$M_{4,5}$, Ti-$L_{2,3}$, Ca-$L_{2,3}$, and O-K edges; the resulting effective energy resolution was limited by the detector point spread function. The convergence and collection semi-angles were 32 and 37 mrad, respectively. The estimated t/lambda value was 0.29, based on the integration of zero loss and plasmon peaks from low loss EELS data acquired immediately following the core-loss EELS acquisitions; consequently, it was deemed unnecessary to treat the data for multiple scattering effects and no further data processing was applied. Figures 3(c) – 3(g) reveal intensity maps (colored and normalized to 0 1 for clarity) for the Pb-M_4, Ba-$M_{4,5}$, Ti-$L_{2,3}$, Ca-$L_{2,3}$, and O-K EELS edges, respectively. These maps were produced by integrating the intensity of the ionization edges at each pixel over a suitable energy window (typically 40 eV), beyond the edge onsets, after subtraction of the continuous decaying background using a power law model.

The most striking feature of the EELS maps is the segregation of Pb, most obvious within a 10–15 nm region spanning across the grain boundary [Fig. 3(c)], whilst Ba appears to be significantly reduced within the same length scale [Fig. 3(d)]. Meanwhile, elemental maps for the remaining elements (Ti, Ca, and O) indicate a homogeneous chemical distribution [Figs. 3(e) – 3(g)]. This means that the composition of these remains unchanged when compared to that of the grain interior. Complementary energy dispersive x-ray (EDX) elemental maps were also acquired, which show good agreement with the EELS data (Fig. S1 in the supplementary material). The Pb segregation and Ba reduction observed here can be assumed to be attributed to A-site substitutions within the ABO_3 perovskite structure. Grain boundaries are well known for their disordered nature, formed by structural defects or dislocation cores,[24] and Pb being more volatile could be attracted to these defective (and highly strained) areas during sintering,[25] hence explaining the chemical heterogeneity observed here. It should be noted that the extent of Pb segregation could differ from one grain to another due to each grain developing slightly different strain gradients during the sintering process.[26] An example of this is observed in Fig. 3(c), where more segregation of Pb is observed in the top grain. Other grain boundaries were analyzed, with different neighboring grain orientations and relative tilt angles, all demonstrating similar results.

As previously mentioned, PTCR ceramics have rich microstructures that are highly sensitive to chemistry and processing conditions, making them complex ceramics to analyze. Previous studies have shown rich structural heterogeneity between grains, where grain boundaries with high lattice disruption and incoherency are a common feature.[5] This lattice disruption makes high resolution imaging of grain boundaries quite challenging, including direct mapping of the polarization across them. Another approach to access similar information is to study the local electronic structure through a detailed analysis of the Ti–O octahedral distortions. Hence, to determine the effect that chemical inhomogeneity has on the electronic structure across the grain boundary, atomic-scale EELS measurements were carried out and more specifically, the electron-energy loss near-edge fine structure (ELNES) of the acquired spectra was examined for changes indicative of electronic structure reconfiguration, focusing on the Ti and O signals. The Ti and O ELNES contain key information about octahedral distortions within the crystal structure as electron energy loss spectra reflect the density of unoccupied states of the material and can thus be used to identify changes in valence and atomic bonding.[27–29] Figure 4(a) is a high resolution high-angle annular dark-field (HAADF) image containing the grain boundary shown in Fig. 3, where EEL spectra have been extracted from 25 positions. Each extracted spectrum spans over an average of eight unit cells, parallel to the interface. A dispersion of 0.2 eV/channel was used in order to acquire simultaneously the Ti and O edges resulting in an effective energy resolution of 0.58 eV. The O-K edge shown in Fig. 4(b) is perhaps the most challenging edge to characterize in oxides due to its multiple peaks that originate from the oxygen bonding to both A- and B-site cations; however, even subtle differences in the peaks represent a change in the chemistry and in the electronic structure.[30] The most striking feature observed here is a gradual shift in the peak marked with an asterisk. This peak is recognized to arise from the hybridization of the O-2p orbitals with states attributed to the A-site cation,[31] making it possible to distinguish a chemical

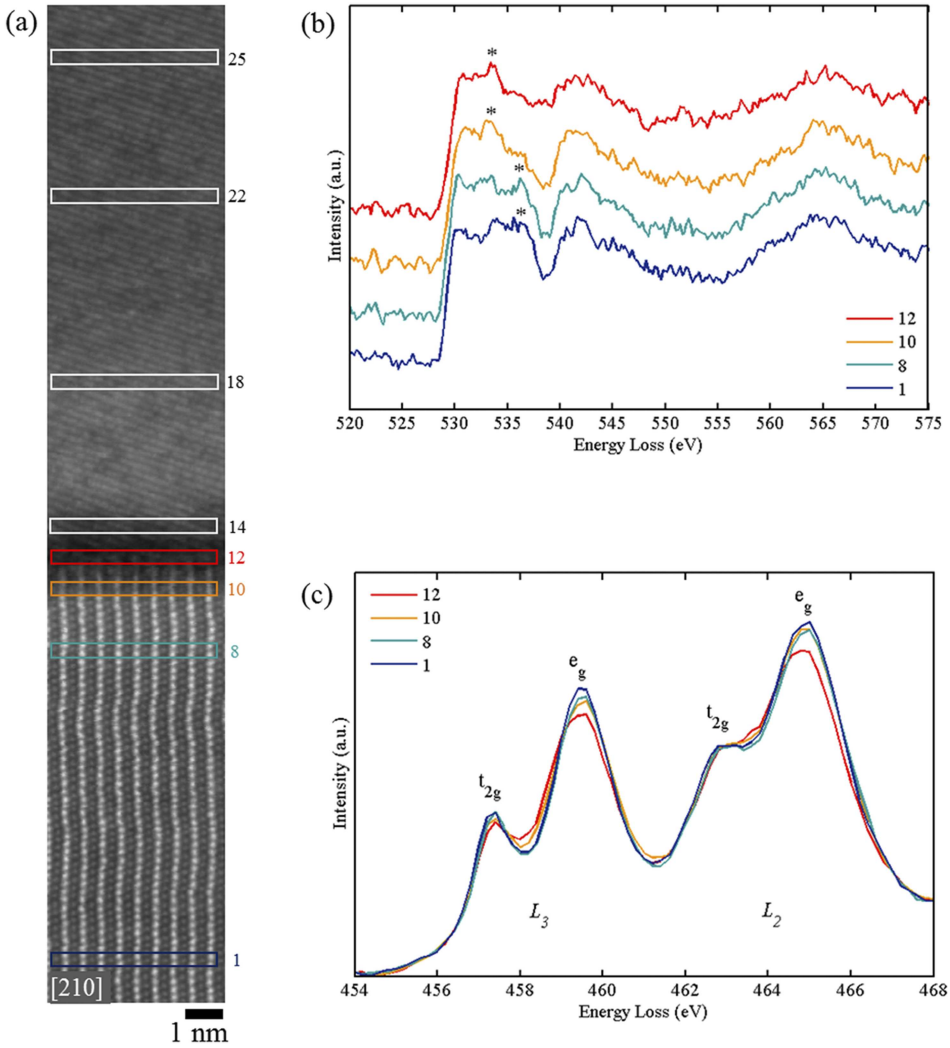

FIG. 4. ELNES for O-K and Ti-$L_{2,3}$ edges. High resolution HAADF image of a single grain boundary where spectra have been extracted from highlighted numbered regions (a). For clarity only selected regions are shown here but the full range can be seen in Fig. S2. O-K edge (b) and Ti-$L_{2,3}$ edge (c) extracted from positions 1, 8, 10, and 12.

transition in the A-site (Ba, Pb, and Ca). The largest shift of this peak occurs on approaching the grain boundary, leading to a spectrum shape which has a remarkable resemblance to the O-K edge of bulk PTO.[31] This shift confirms how the bonding nature of oxygen is altered as a function of the change in the A-site chemistry between the more BTO-like bulk-of-grain regions compared to the Pb-rich grain boundary regions. To rule out any orientation effects influencing the ELNES the same area was measured twice, once with the bottom grain tilted onto zone axis, and once with the top grain tilted onto zone axis, similar features were seen either side of the grain boundary (Fig. S2 in the supplementary material). Although it is well known that oxygen vacancies can be a common feature in perovskites, our data did not show any resemblance to reported, simulated, or experimental spectra where O vacancies were considered.[32,33] Thus, within the signal-to-noise ratio (SNR) of our data, ELNES does not provide any reason to believe that O vacancies, and inhomogeneity in oxygen vacancy distribution, play a major role in our observations.

Furthermore, we investigate changes in the crystal and electronic structure along the grain boundary by analyzing the Ti-$L_{2,3}$ edge, associated to the Ti–O octahedral distortions. The splitting of the $L_{2,3}$ edge due to spin-orbit coupling is attributed to electron excitations from the Ti-$2p_{3/2}$ (L_3 edge) and $2p_{1/2}$ (L_2 edge) states into unoccupied Ti-3d states near the Fermi level.[30,34,35] Due to the octahedral symmetry of the Coulomb potential, the L_3 and L_2 edges are each split into two further peaks

representing the molecular orbitals e_g and t_{2g}, where the separation is known as the crystal field splitting (CFS). The lower energy t_{2g} orbitals point toward the faces of the TiO_6 octahedron (xy, xz, and yz), whereas the e_g higher energy orbitals point toward corners containing O anions ($d_{x^2-y^2}$ and d_{z^2}). It is well accepted that in a cubic symmetry crystal (e.g. $SrTiO_3$)[36,37] the energies of the orbitals in the e_g peak are degenerate, presenting a single sharp peak. However, for a tetragonal symmetry (e.g., BTO and PTO), the e_g peak shows a clear splitting due to the breaking of degeneracy. Given that the EELS signal is highly sensitive to the subtle changes in the TiO_6 octahedron, we can expect a change in the Ti-$L_{2,3}$ edge between the more BTO-like grain interior compared to the Pb-rich grain boundary regions. The Ti-$L_{2,3}$ spectra [Fig. 4(c)] show significant trends on approaching the grain boundary, such as a decrease in ratio between the t_{2g} and e_g peaks, and a broadening of the e_g peak, most obvious when comparing the spectrum from within the grain (position 1) and the grain boundary (position 12). Due to the energy resolution in experiment, the splitting of the e_g peak is not easily resolved; however, it is well established that this splitting effect is observed as an e_g peak broadening.[31,36,38]

As the e_g peak broadens, the CFS is reduced and an inverse relationship between CFS and the average Ti–O bond length is established.[37,39] Due to the clear chemical inhomogeneity in this ceramic and the intrinsic change in symmetry between BTO, PTO, and CTO, the CFS is expected to change.[30,31,37] It has been shown that bulk BTO has a higher CFS compared to bulk PTO,[36,38] and therefore a quantitative analysis of the CFS across the grain boundary was carried out here. The contribution from CTO can be disregarded since the Ca content is constant. Figure 5 displays the CFS trend of the L_3 edge for each of the spectra positions in Fig. 4. The CFS estimate of the L_3 edge is more accurate than that for the L_2 edge, due to a more accurate pre-edge background fitting and higher signal levels, and therefore only the former is shown in Fig. 5. The CFS was calculated by fitting Gaussians to the respective peaks and measuring the center-to-center displacement (see left inset in Fig. 5 as an example) with sub-pixel accuracy. From our measurements, a decrease in CFS is clearly observed approaching the grain boundary. The decrease in CFS (Δ0.14 eV) confirms a tetragonal distortion of the TiO_6 octahedron and points towards an enhanced noncentrosymmetric position of the Ti cation from the lowering of energy of the d_{z^2} orbitals,[37] represented by L_3-e_g peak

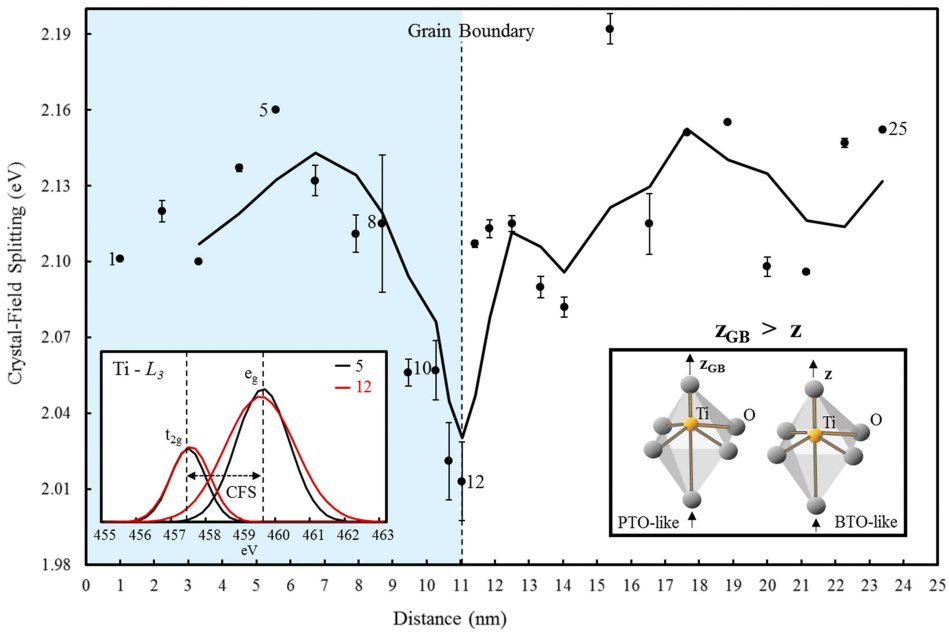

FIG. 5. CFS of Ti-L_3 edge spanning 25 nm across the grain boundary presented in Fig. 4. CFS was calculated by fitting Gaussian curves to the e_g and t_{2g} peaks and measuring the center-to-center displacement, as exemplified in the left inset. Position markings are in reference to those in Fig. 4. Schematics of octahedral distortion are depicted for the BTO-like and PTO-like regions in the right inset.

broadening. Thus, a transition between a BTO-like grain interior and a PTO-rich grain boundary region has been further determined by a decrease in CFS. The Ti valence state was also examined over various datasets; however, the small changes observed here were inconclusive since they lay within the error limit (Fig. S3 in the supplementary material).

Even though BTO and PTO share a similar perovskite structure, they show drastic differences in spontaneous polarization, BTO having a magnitude of 26 μC/cm^2 and PTO > 50 μC/cm^2.[40] Thus, it can be expected that PTO-rich grain boundaries will have a higher net polarization normal to the grain boundaries compared to the more BTO-like grain interior, creating a localized polarization step.

According to the modified Heywang-Jonker model, the barrier potential observed at the grain boundary is given by Eq. (3). The polydomain nature of the grains will induce a population of polar discontinuities across the grain boundaries and overall, a great variety in polar discontinuity conditions will exist; this creates a number of low and high resistance paths which act electrically in parallel at every grain boundary. Current will flow preferentially across the regions in which the potential barrier has been lowered, as a result of specific polar discontinuity states, and hence an overall low grain boundary resistance state will result. It is the regions in which polar discontinuities lead to the largest reduction in local boundary height that therefore ultimately dictate the effective barrier height of the grain boundary as a whole. Variations in barrier heights between grains should exist but not vary dramatically.

Therefore, the presence of a Pb-rich (PTO-like) phase at the grain boundary will contribute an increased magnitude of polarization compared to the bulk, and hence further bring down the potential barrier at the grain boundary, below T_C. In turn, this decrease in the potential barrier will result in a reduction of the resistivity as described by Eq. (2). Upon undergoing the ferroelectric to paraelectric phase transition at T_C, where the spontaneous polarization no longer exists, depletion regions and resistive barriers at the grain boundaries are restored leading to a high resistive grain boundary state. Thus, the existence of a PTO-rich region would suggest an enhanced spontaneous polarization at the boundary, fully justifying the existence of the optimized PTCR effect in this ceramic.

To summarize, nanoscale microscopy techniques have been employed to establish the link between chemical inhomogeneity and electronic structure across grain boundaries in a BTO based commercially available PTCR ceramic: BTO-PTO-CTO. A segregation of Pb and a corresponding depletion of Ba near grain boundaries was observed. Furthermore, a decrease in CFS suggestive of octahedral distortion was identified via changes in Ti-$L_{2,3}$ and O-K ELNES features approaching the grain boundary, thus revealing a more Pb-rich region within 10–15 nm from the grain boundary, suggestive of a polarization gradient. This work links the chemical and electronic heterogeneity of the studied PTCR ceramic to the changes in potential barrier at the grain boundary, theorized by the Heywang-Jonker model. The results shown here have been evaluated on a specific ceramic composition but are relevant to the general family of PTCR ceramics. The central idea that a confined interfacial region, with higher spontaneous polarization that reduces the grain boundary barrier potential, augments electronic transport and enhances the magnitude of resistivity jump at T_C is novel by itself. While providing an insight into the mechanistic origin of the reduction in potential barrier at grain boundaries in the low temperature ferroelectric phase, this idea also offers a novel route towards engineering PTCR ceramics in which an interface layer of higher spontaneous polarization could be created to produce better performing PTCR devices.

See supplementary material for EDX imaging and additional EEL spectra of grain boundaries and grain interior.

The authors thank Roger Whatmore, from Imperial College London, and Robert Twiney, from Amphenol Advanced Sensors, for supplying the PTCR ceramics. K.M.H., A.M.D., and M.A. acknowledge support from the Engineering and Physical Sciences Research Council (EPSRC) for Ph.D. studentship funding. K.M.H. and M.A. acknowledge support from SuperSTEM, the U.K.'s National Facility for Aberration Corrected STEM, funded by the EPSRC.

[1] B. M. Kulwicki, J. Phys. Chem. Solids **45**, 1015 (1984).
[2] D. Y. Wang and K. Umeya, J. Am. Ceram. Soc. **73**, 669 (1990).
[3] J. Nowotny and M. Rekas, Ceram. Int. **17**, 227 (1991).
[4] Y. L. Chen and S. F. Yang, Adv. Appl. Ceram. **110**, 257 (2011).

[5] R. D. Roseman and N. Mukherjee, J. Electroceram. **10**, 117 (2003).
[6] G. Goodman, J. Am. Ceram. Soc. **46**, 48 (1963).
[7] W. Heywang, J. Am. Ceram. Soc. **47**, 484 (1964).
[8] G. H. Jonker, Solid-State Electron. **7**, 895 (1964).
[9] J. Daniels and R. Wernicke, Philips Res. Rep. **31**, 544 (1976).
[10] B. M. Kulwicki and A. J. Purdes, Ferroelectrics **1**, 253 (1970).
[11] J. E. Ralph, J. P. Gowers, and M. R. Burgess, Appl. Phys. Lett. **41**, 343 (1982).
[12] D. C. Sinclair and A. R. West, J. Appl. Phys. **66**, 3850 (1989).
[13] F. D. Morrison, D. C. Sinclair, and A. R. West, Int. J. Inorg. Mater. **3**, 1205 (2001).
[14] S. M. Gheno, H. L. Hasegawa, and P. I. Paulin Filho, Cerâmica **53**, 200 (2007).
[15] L. Affleck and C. Leach, J. Eur. Ceram. Soc. **25**, 3017 (2005).
[16] J. Hou, Z. Zhang, W. Preis, W. Sitte, and G. Dehm, J. Eur. Ceram. Soc. **31**, 763 (2011).
[17] M. A. Zubair and C. Leach, J. Eur. Ceram. Soc. **30**, 107 (2010).
[18] A. M. Douglas, A. Kumar, R. W. Whatmore, and J. M. Gregg, Appl. Phys. Lett. **107**, 172905 (2015).
[19] D. Hill and H. Tuller, in *Ceramic Sensors: Theory and Practise, Ceramic Materials for Electronics,* edited by R. Buchanan (Marcel Dekker Inc., New York, 1991).
[20] D. Voltzke, H. P. Abicht, E. Pippel, and J. Woltersdorf, J. Eur. Ceram. Soc. **20**, 1663 (2000).
[21] P. Fiorenza, R. Lo Nigro, P. Delugas, V. Raineri, A. G. Mould, and D. C. Sinclair, Appl. Phys. Lett. **95**, 142904 (2009).
[22] M. S. Silva, S. T. Souza, D. V. Sampaio, J. C. A. Santos, E. J. S. Fonseca, and R. S. Silva, J. Eur. Ceram. Soc. **36**, 1385 (2016).
[23] D. C. Sinclair and A. R. West, J. Mater. Sci. **29**, 6061 (1994).
[24] P. Prabhumirashi, V. P. Dravid, A. R. Lupini, M. F. Chisholm, and S. J. Pennycook, Appl. Phys. Lett. **87**, 121917 (2005).
[25] M. Arredondo, Q. M. Ramasse, M. Weyland, R. Mahjoub, I. Vrejoiu, D. Hesse, N. D. Browning, M. Alexe, P. Munroe, and V. Nagarajan, Adv. Mater. **22**, 2430 (2010).
[26] Q. Yin, B. Zhu, and H. Zeng, *Microstructure, Property and Processing of Functional Ceramics* (Metallurgical Industry Press: Springer Verlag, Berlin, 2009).
[27] L. A. Grunes, R. D. Leapman, C. N. Wilker, R. Hoffmann, and A. B. Kunz, Phys. Rev. B **25**, 7157 (1982).
[28] D. H. Pearson, C. C. Ahn, and B. Fultz, Phys. Rev. B **47**, 8471 (1993).
[29] J. Graetz, C. C. Ahn, H. Ouyang, P. Rez, and B. Fultz, Phys. Rev. B **69**, 235103 (2004).
[30] E. Stoyanov, F. Langenhorst, and G. Steinle-Neumann, Am. Mineral. **92**, 577 (2007).
[31] A. Torres-Pardo, A. Gloter, P. Zubko, N. Jecklin, C. Lichtensteiger, C. Colliex, J. Triscone, and O. Stephan, Phys. Rev. B **84**, 220102 (2011).
[32] D. Woodward, I. Reaney, G. Yang, E. Dickey, and C. Randall, Appl. Phys. Lett. **84**, 4650 (2004).
[33] D. Batuk, M. Batuk, A. A. Tsirlin, J. Hadermann, and A. M. Abakumov, Angew. Chem., Int. Ed. **54**, 14787 (2015).
[34] R. D. Leapman, L. A. Grunes, and P. L. Fejes, Phys. Rev. B **26**, 614 (1982).
[35] F. M. F. Degroot, Z. W. Hu, M. F. Lopez, G. Kaindl, F. Guillot, and M. Tronc, J. Chem. Phys. **101**, 6570 (1994).
[36] E. Eberg, A. T. J. van Helvoort, R. Takahashi, M. Gass, B. Mendis, A. Bleloch, R. Holmestad, and T. Tybell, J. Appl. Phys. **109**, 034104 (2011).
[37] D. Park, A. Herpers, T. Menke, M. Heidelmann, L. Houben, R. Dittmann, and J. Mayer, Microsc. Microanal. **20**, 740 (2014).
[38] J. M. Zhang, A. Visinoiu, F. Heyroth, F. Syrowatka, M. Alexe, D. Hesse, and H. S. Leipner, Phys. Rev. B **71**, 064108 (2005).
[39] A. S. Sefat, G. Amow, M. Y. Wu, G. A. Botton, and J. E. Greedan, J. Solid State Chem. **178**, 1008 (2005).
[40] M. E. Lines and A. M. Glass, *Principles and Applications of Ferroelectrics and Related Materials* (Oxford University Press, New York, 1977).